Characterizing Large-Scale Receptor Clustering on the Single Cell Level: A Comparative Plasmon Coupling and Fluorescence Superresolution Microscopy Study

Sandy Zhang and Björn M. Reinhard*

Department of Chemistry and The Photonics Center, Boston University,

Boston, MA 02215

*E-mail: bmr@bu.edu

ABSTRACT: Spatial clustering of cell membrane receptors has been indicated to play a regulatory role in signal initiation and the distribution of receptors on the cell surface may represent a potential biomarker. To realize its potential for diagnostic purposes, scalable assays capable of mapping spatial receptor heterogeneity with high throughput are needed. In this work, we use gold nanoparticle (NP) labels with an average diameter of 72.17 $\pm$ 2.16 nm as bright markers for large-scale epidermal growth factor receptor (EGFR) clustering in hyperspectral plasmon coupling microscopy and compare the obtained clustering maps with those obtained through fluorescence superresolution microscopy (direct stochastic optical reconstruction microscopy, dSTORM). Our dSTORM experiments reveal average EGFR cluster sizes of 172 $\pm$ 99 nm and 150 $\pm$ 90 nm for MDA-MB-468 and HeLa, respectively. The cluster sizes decrease after EGFR activation. Hyperspectral imaging of the NP labels shows that differences in the EGFR cluster sizes are accompanied by differences in the average separations between electromagnetically coupled NPs. Due to the distance-dependence of plasmon coupling, changes in the average interparticle separation result in significant spectral shifts. For the experimental conditions investigated in this work, hyperspectral plasmon coupling microscopy of NP

labels identified the same trends in large-scale EGFR clustering as dSTORM, but the NP imaging approach provided the information in a fraction of the time. Both dSTORM and hyperspectral plasmon coupling microscopy confirm the cortical actin network as one structural component that determines the average size of EGFR clusters.

KEYWORDS: *gold nanoparticles, receptor clustering, EGFR, single cell analytics, signaling, bioplasmonics*

The epidermal growth factor receptor (EGFR or HER1/ERbB1) is a cell surface receptor tyrosine kinase (RTK) that plays a fundamental role in cell growth and proliferation, while its dysregulation is associated with a broad range of cancers.[1] In the asymmetric kinase dimer, interactions between the acceptor and receiver kinase are responsible for phosphorylating the C-terminus of the receptor and initiating downstream signaling. Ligand binding to the extracellular region induces receptor dimerization and conformational changes that propagate across the membrane to induce phosphorylation in the intracellular region.[2,3] Research into EGFR activation has long focused on the crucial step of EGFR dimerization,[4,5] but it is now clear that EGF-induced EGFR oligomerization[6–13] and the formation of extended clusters may also have important regulatory functions.[14–23] In order to probe the biological role of spatial receptor heterogeneity and to utilize it as a diagnostic biomarker, it is crucial that methods are available to detect, characterize, and quantify receptor clustering, ideally on the single cell level with high throughput. This manuscript focuses on the characterization of large-scale receptor clustering, with typical effective radii of several tens of nanometers[10,14,24,25], and thus still too small to be resolved by conventional diffraction-limited optical microscopy techniques[24,26]. To obtain information about the spatial distribution of plasma membrane EGFR on the nanoscale,

fluorescence-based optical methods such as brightness analysis[26,27], near-field microscopy[14], multi-color optical tracking[28–30], and far-field superresolution fluorescence microscopy[31–33] have been used. Diffraction limited approaches, such as brightness analysis, provide only information about the number of receptors in a diffraction-limited spot with no direct information about the spatial clustering of the receptors on shorter length scales. In contrast, fluorescence superresolution microscopy techniques that utilize single-molecule photoactivation or photoswitching of fluorophores, can map the receptor distribution below the diffraction limit. However, single-molecule localization microscopy (SMLM) techniques such as direct stochastic optical reconstruction microscopy (dSTORM) typically require acquisition of thousands of image frames[34–37] to reconstruct a superresolution image. The associated long acquisition times limit experimental throughput[34] and make a statistical analysis of receptor clustering in a heterogeneous cell ensemble challenging. Similarly, near-field scanning microscopy and multi-color tracking also have limitations in experimental throughput. In addition to method-specific challenges, fluorescence-based approaches in general are subject to restrictions with regard to the brightness and photostability of organic dyes. These fundamental limitations have spurred interest in alternative, non-fluorescence based optical approaches for detecting large-scale receptor clustering in the plasma membrane based on the distance-dependent plasmon coupling between metal nanoparticle (NP) immunolabels.[38–44] Metal NPs have large optical cross-sections and offer superb photophysical stability.[45] Plasmon coupling between metallic NPs can be detected in the far-field through elastic or inelastic scattering spectroscopy. The latter utilizes an increase in the Raman signal intensity of dyes bound to the NP when they form electromagnetic hot spots,[46–48] while the former detects shifts of the plasmon resonance.[38,49–52] The work performed so far successfully demonstrated the optical detection of NP label clustering due to binding to specific

receptors in the membrane, including EGFR, but the detected clustering information have not been systematically compared with those obtained with an alternative method capable of imaging the receptor distribution below the diffraction limit. Additionally, the relationship between the spatial heterogeneity of the targeted surface protein and the spectral information of the NP labels remains insufficiently characterized. In this manuscript, we address this knowledge gap and characterize the relationship between large-scale EGFR clustering and the optical plasmon coupling signal by using superresolution microscopy (dSTORM) of fluorescently labeled EGFR as a validation method and compared the obtained clustering information from both imaging techniques with each other. Subsequently, we apply both imaging approaches to test the role of the cortical actin network in patterning large-scale EGFR clustering.

RESULTS

Superresolution dSTORM Imaging of EGFR Clustering.

To investigate the spatial heterogeneity of EGFR "clusters", where a cluster is defined as a membrane region enriched in EGFR, we used dSTORM imaging with an average localization precision of 27 nm and spatial resolution of 62 nm (**Figure S1**). All experiments in this work were performed with two different cell lines; the human cervical cancer cell line HeLa with a physiological EGFR expression level (5×10^4 receptors/cell)[53] and the triple negative breast cancer cell line MDA-MB-468, as an example of an EGFR overexpressor (1×10^6 receptors/cell)[54]. **Figure 1A** shows i.) a reconstructed dSTORM image of fluorescently labeled EGFR of an entire cell, ii.) a magnified 4 µm × 4 µm section of the reconstructed image, iii.) the corresponding pseudo-colored cluster map (red areas

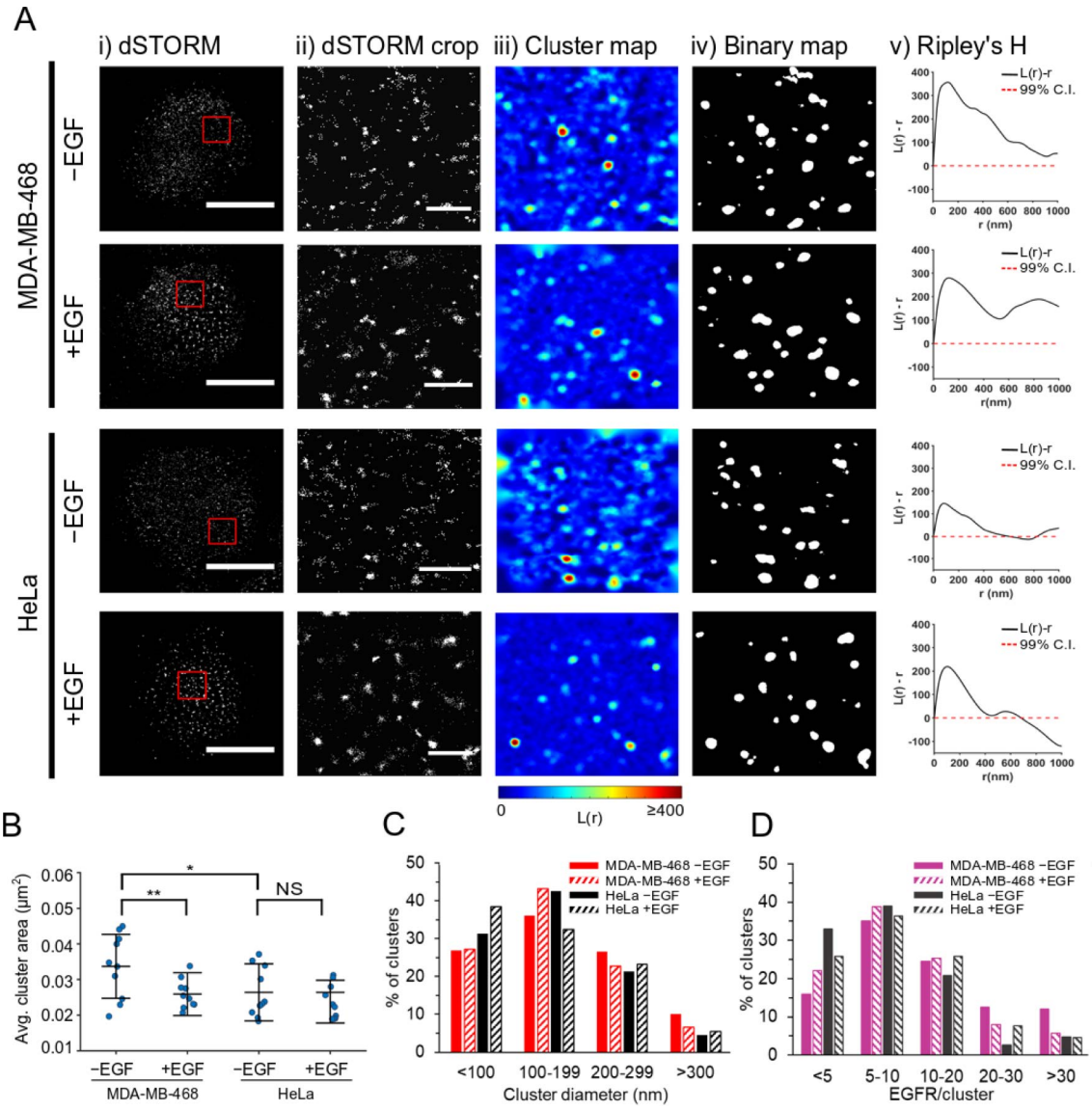

Figure 1: (A) (i) Representative reconstructed dSTORM images of MDA-MB-468 (−/+) EGF (top) and HeLa (−/+) EGF (bottom). Scale bar: 10 μm. **(ii)** The 4 μm × 4 μm regions outlined in red are enlarged and shown with the corresponding **(iii)** cluster map according to a psuedocolor scale bar, **(iv)** thresholded binary maps, and **(v)** Ripley's *H*-distributions. Scale bar: 1 μm. **(B)** Plot of average cluster area for all experimental conditions. Each data point represents the average cluster area for two 4 μm × 4 μm regions per cell for a total of 10 cells each. Lines represent average ± SD. $^{*}P < 0.05$, $^{**}P < 0.01$, and NS (not significant) by unpaired two-sample *t*-test. **(C)** Histogram of EGFR cluster diameter distribution. **(D)** Histogram of EGFR per cluster. The data presented in **(B-D)** were from 10 cells (3 independent experiments).

indicate locations of high EGFR density), as well as the associated iv.) thresholded binary cluster map and v.) Ripley's *H*-function as a function of separation for from (top to bottom) MDA-MB-468 (−/+) EGF and HeLa (−/+) EGF.

The local clustering of EGFR is illustrated in the cluster maps shown in **Figure 1Aiii**, which contain the value of Ripley's *L*-function evaluated at a spatial scale of r = 80 nm. The pseudo-colored cluster maps were thresholded by an L(r) cutoff value to define clusters and the resulting binary cluster maps are shown in **Figure 1Aiv**. The Ripley's *H*-functions in **Figure 1Av** for MDA-MB-468 (−/+) EGF are quite broad and remain positive on length scales up to 1000 nm, whereas in HeLa (−/+) EGF, the positive spatial correlation disappeared on length scales beyond 600 nm. Importantly, the *H*-functions peak at separations between 80 and 120 nm for MDA-MB-468 and HeLa (−/+) EGF, which indicates strong spatial EGFR clustering on the length scale of tens of nanometers.

Figure 1B summarizes the average cluster area (obtained from the binary cluster map) for two randomly selected 4 μm × 4 μm areas in the central region of 10 cells. The average cluster area for MDA-MB-468 decreases significantly from 0.034 ± 0.009 μm^2 to 0.026 ± 0.006 μm^2 after EGF addition. For HeLa, a slight decrease from 0.026 ± 0.008 μm^2 to 0.024 ± 0.006 μm^2 is observed after EGF addition, but the difference in the average cluster area (−/+) EGF is not statistically significant.

The cluster diameter histograms in **Figure 1C** provide an overview of the distribution of effective cluster diameters of 0-99 nm, 100-199 nm, 200-299 nm, and > 300 nm for the investigated conditions. For both MDA-MB-468 and HeLa (- EGF), clusters with a diameter between 100 – 199 nm have the highest probability, but the contribution from larger clusters are higher for MDA-MB-468 -EGF than for all other conditions. For MDA-MB-468 +EGF, the contribution from these larger cluster diameters decreases and the contribution from 100 - 199 nm is further increased. After EGF addition to HeLa, the contribution from clusters with a diameter < 100 nm is increased, primarily at the expense of decrease in clusters with diameters between 100 - 199 nm. The average EGFR cluster

sizes for MDA-MB-468 and HeLa (–/+) EGF were determined as 172 ± 99 nm / 155 ± 91 nm and 150 ± 90 nm / 145 ± 90 nm, respectively.

The number of localizations in each cluster obtained from the binary map can be used to estimate the number of EGFR per cluster if one accounts for the number of Alexa-647 dyes conjugated to an individual anti-EGFR antibody. The resulting numbers of EGFR / cluster for the different experimental conditions are shown in **Figure 1D**. In the absence of stimulation, MDA-MB-468 contains an average of 15 EGFR/cluster compared with only 10 EGFR/cluster for HeLa. The over-expressing MDA-MB-468 has a higher EGFR expression level than HeLa, which corresponds to an increase in percentage of intermediate to larger sized clusters containing more than 10 EGFR. Additionally, activation of EGFR with free EGF results in a higher number of clusters with < 10 EGFR for both cell lines. Overall, a higher number of clusters with less EGFR is consistent with the increase in small to intermediate-sized clusters with diameters less than 199 nm and a decrease in the average cluster area.

Hyperspectral Plasmon Coupling Microscopy for Characterizing EGFR Heterogeneity.

We hypothesize that spectral imaging of NPs targeted at EGFR can detect large-scale EGFR clustering and discern between different levels of clustering **(Figure 2A)**. The distance-dependent plasmon coupling between gold NP labels[55–59] with diameter, D, forms the basis for the spectral detection of large-scale receptor clustering. NPs can bind to two EGFR proteins without structural interference if the interparticle separation is $d > D$. If binding to the EGFR localizes two NPs within the range $D < d < 2D$, the NPs are sufficiently close for electromagnetic coupling to occur and the resulting hybridization of the plasmons[60,61] induces a spectral red-shift as a quantifiable observable of clustering

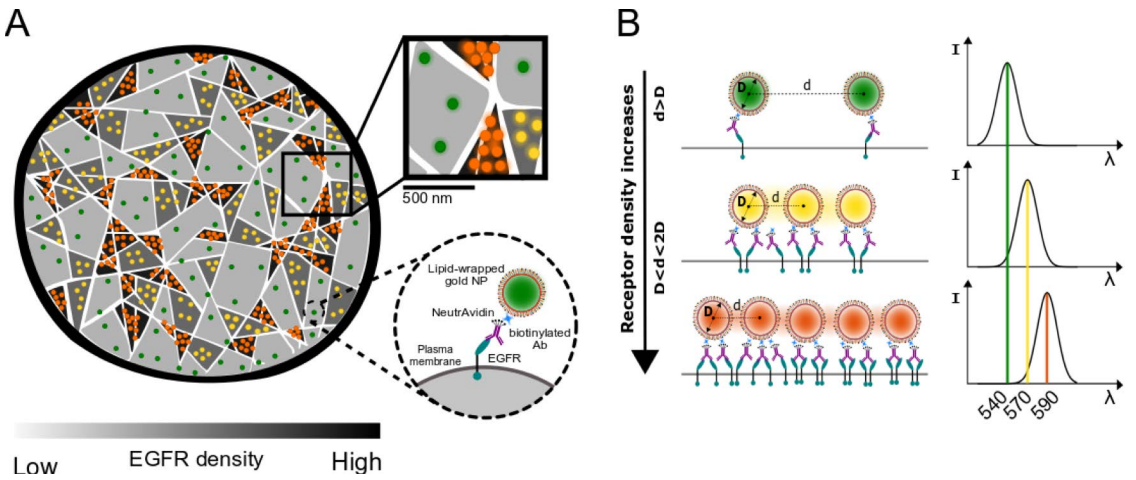

Figure 2. (A) Schematic illustration of using gold NP labels to detect large-scale EGFR clustering. As receptor density increases, so does the NP density. The inset on the upper right illustrates a model of the cortical actin network (white) as a structure defining component that patterns large-scale EGFR clustering. Dashed circle on the lower right shows the immunolabeling strategy based on biotin-avidin binding between biotinylated anti-EGFR antibody (Ab) and biotinylated lipid-wrapped gold NPs. **(B)** A decrease in the average interparticle separation (*d*) of NP labels with diameter (*D*) leads to a spectral red-shift, which is an observable of receptor clustering.

(**Figure 2B**). As the probability of receptors with separations $d < 2D$ increases with EGFR clustering, a spectral red-shift of the resonance wavelength of the NP labels relative to that of an individual NP is an indicator of a local increase in EGFR density. Additional factors, such as the ratio of NP diameter to EGFR cluster size and the number of NPs bound per cluster determine the magnitude of the experimentally observed spectral shift. In a previous study, Abulrob *et al.* used near-field scanning optical microscopy to characterize the heterogeneous distribution of EGFR in the plasma membrane of HeLa cells and reported an average cluster size of approximately 150 nm.[14] Informed by this number and our dSTORM results, which revealed average cluster sizes between 145 ± 90 nm and 172 ± 99 nm for the experimental conditions tested, we used lipid-wrapped gold NPs with a diameter of 72.17 ± 2.16 nm as labels in this work since they are small enough to allow binding of multiple NPs in EGFR-enriched membrane domains, but at the same time, have large scattering cross-sections to ensure a strong contrast relative to the

cellular environment.[62] The NPs were wrapped with a thin membrane assembled primarily from 1,2-dipalmitoyl-*sn*-glycero-3-phosphocholine (DPPC), cholesterol, and a small fraction of biotinylated lipid. The lipids were tethered to the NPs *via* octadecanethiol as described previously.[63–65] The incorporation of biotin into the membrane of the NPs facilitated a biotin-avidin based immunolabeling of EGFR as outlined in **Figure 2A**.

Optical Analysis of EGFR Heterogeneity through Plasmon Coupling between NP labels.

In **Figure 3A**, digital color images of NP labels (immobilized on glass) before and after incubation with cells have the characteristic green color of monodisperse gold NPs. We independently verified that incubation with cells did not systematically change the hydrodynamic diameter and UV-Vis spectra of unbound NP labels (**Figure S2**). **Figure 3B** shows digital color images of NP labels bound to MDA-MB-468 and HeLa cells before and after addition of 10 nM EGF. This concentration is 10 times higher than the dissociation constant of EGF to EGFR and ensures stoichiometric binding of ligand to the targeted receptor.[53,66] Tests of the spatial randomness of the distribution of the optically discernable NPs performed with the Hopkins statistic, H,[67] for 50 cells per experimental condition (**Figure S3**) reveal nearly random NP distributions ($H \approx 0.5$) on length scales above the diffraction limit at $\lambda = 540$ nm for all experimental conditions. However, the apparent difference in color of the NPs targeted to EGFR on MDA-MB-468 and, in particular, to HeLa when compared with the unbound controls suggests clustering on length scales below the diffraction limit. To independently confirm NP clustering on sub-diffraction limit length scales, we analyzed the NP-labelled cells after fixation through scanning electron microscopy (SEM) at a much higher spatial resolution (**Figure S4**). Inspection of the SEM micrographs revealed discrete NP clusters with H values shifted closer to 1, confirming a

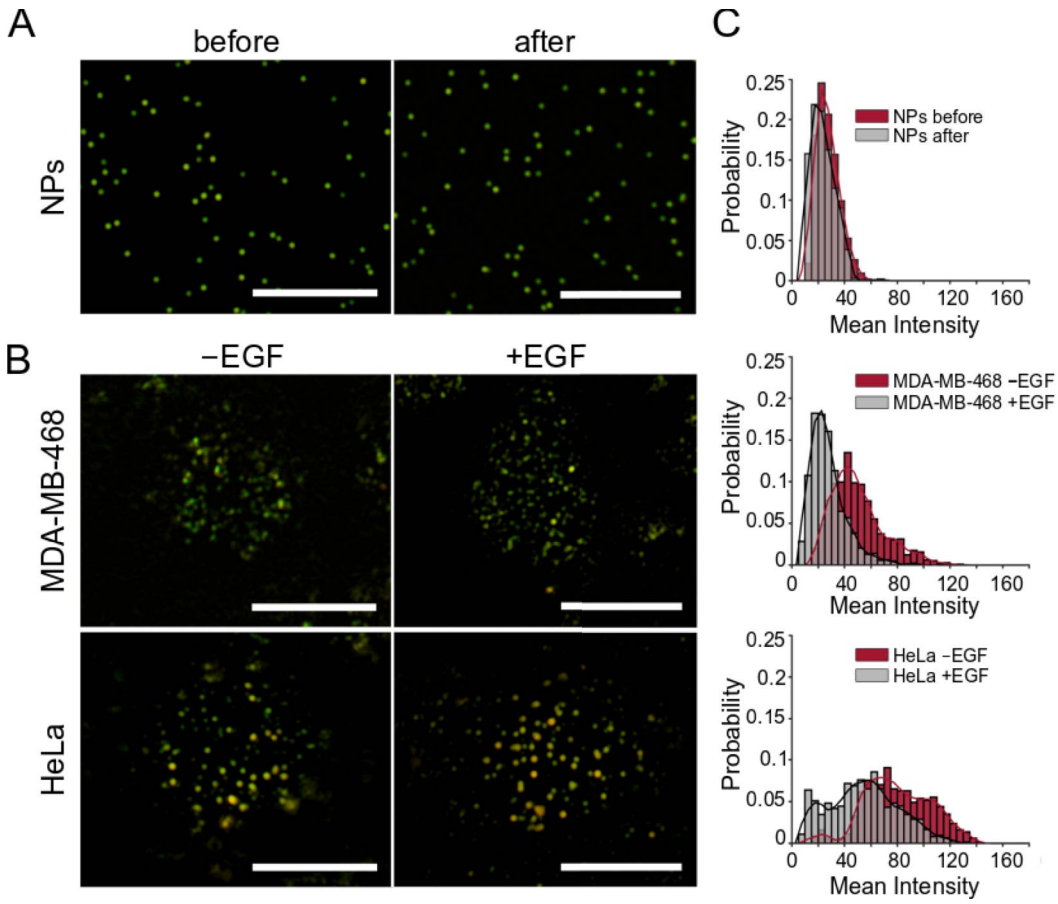

Figure 3. (A) Digital color images of NP labels immobilized on glass before and after incubation with cells. The NP labels are stable as depicted by the characteristic green scattering color. Scale bar: 10 μm **(B)** Digital color images of NP labeled MDA-MB-468 without and with 10 nM EGF stimulation (top) and HeLa without and with 10 nM EGF stimulation (bottom). Scale bar: 10 μm **(C)** Histogram of mean intensity distribution of NP labels for NP controls (top), MDA-MB-468 (−/+) EGF (middle), and HeLa (−/+) EGF (bottom). The data presented in **(C)** were from 50 cells (3 independent experiments).

significant level of clustering of NP labels bound to MDA-MB-468 and HeLa on sub-diffraction limit length scales.

Intriguingly, the color of the NPs bound to HeLa are overall red-shifted relative to those bound to MDA-MB-468 and the NP controls in **Figures 3A** and **B**. This color change indicates a stronger electromagnetic coupling between NP labels for HeLa than for MDA-MB-468. This trend is also consistent with a higher average intensity of NP scatterers[49] on HeLa than on MDA-MB-468 or NP controls (**Figure 3C**). EGFR activation through EGF

decreases the mean scattering intensity for both MDA-MB-468 and HeLa, suggesting less NP clustering after ligand stimulation.

Wide-Field Ratiometric Analysis of NP labels to Quantify EGFR Clustering.

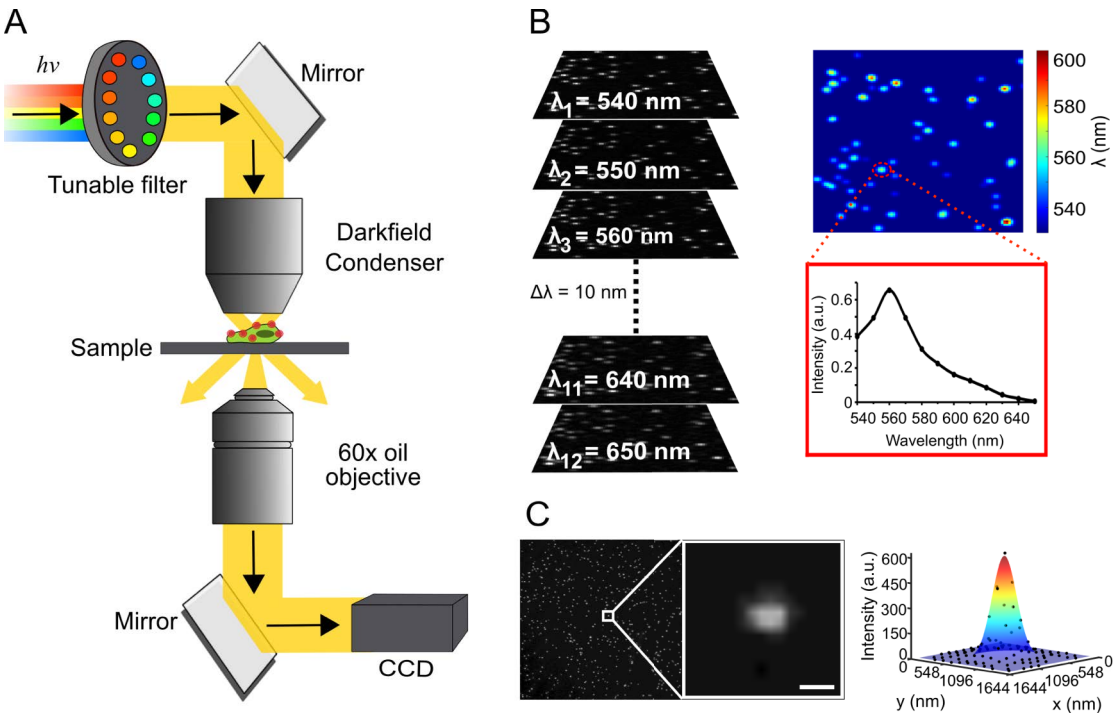

Figure 4: (A) Schematic overview of set-up for hyperspectral plasmon coupling microscopy. **(B)** Acquisition of a monochromatic image from λ = 540-650 nm, every 10 nm, to generate a hyperspectral composite image. Each pixel in the composite image provides complete spectral information of the NP labels. **(C)** Representative CCD image of gold NPs immobilized on glass and an enlarged image showing an individual NP and the corresponding 2D Gaussian fit. Scale bar: 1 µm

To quantify the spectral difference between NP labels bound to HeLa and MDA-MB-468, and to characterize more subtle differences between cells before and after EGFR activation (−/+) EGF, we measured in the next step the spectra of the NP labels using the hyperspectral plasmon coupling microscopy[44,49] approach described in **Figure 4A**. In this technique, a monochromatic image was recorded every 10 nm between 540-650 nm to generate a hyperspectral composite image. Importantly, each pixel in the composite i

mage contains an entire spectrum and information about the relative intensities of NPs from different wavelength channels (**Figure 4B**). The typical spatial resolution (resolving power) of discrete NPs in our set-up was Δx = 651 nm as determined by the full width at half maximum (FWHM) of the fitted point spread function (PSF) of individual NPs **(Figure 4C)**. This imaging method provides spectral and spatial information of all scatterers in the field of view (141 µm × 141 µm at the chosen magnification) with an average localization precision of 1 nm for individual NP scatterers at the chosen acquisition time of 0.1 s. For spectral analysis of NP labels, we determined the resonance wavelength, λ_{peak}, defined as the wavelength channel with the highest intensity, for each NP pixel in the field of view (**Figure 5A**). The distributions for NP labels as synthesized and after recovery from a

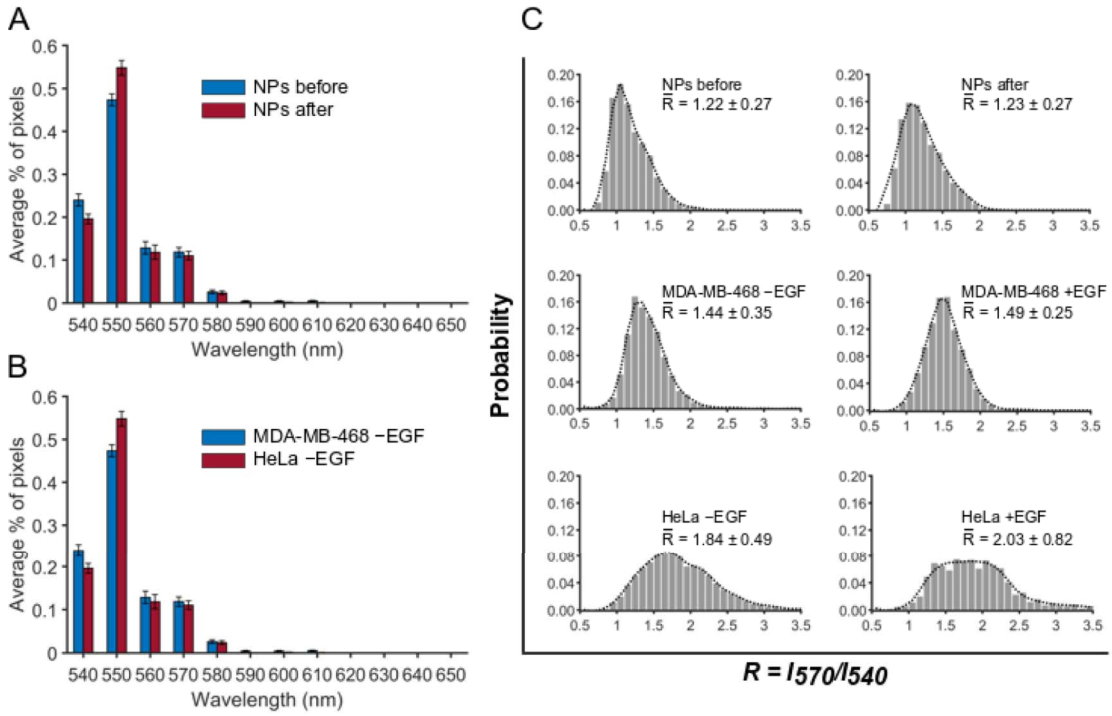

Figure 5: Resonance peak wavelength and ratiometric analysis of NP labels. **(A)** Peak wavelength, λ_{peak}, for NP labels in solution before and after incubation with cells **(B)** λ_{peak} histograms for NP labels bound to MDA-MB-468 and HeLa (−EGF). Error bars in **(A)** and **(B)** are ± s.e.m. **(C)** Histograms of $R = I_{570}/I_{540}$ for NP labels before and after incubation with cells (top row), NPs bound to MDA-MB-468 without and with 10 nM EGF treatment (middle row), and NPs bound to HeLa without and with 10 nM EGF treatment (bottom row). The data presented in **(A-C)** were collected from 50 cells (3 independent experiments).

solution incubated with cells, peak at 550 nm and are nearly identical, confirming the stability of the NP labels. In **Figure 5B**, the λ_{peak} distributions for both MDA-MB-468 and HeLa $(-)$ EGF are broadened to longer wavelengths when compared with NPs immobilized on glass. Compared with NP controls, λ_{peak} = 550 nm still has the highest probability for MDA-MB-468 −EGF, but its value is decreased while the contributions from longer wavelengths have increased. The shift to longer peak wavelengths is strongest for HeLa, for which the frequencies of λ_{peak} = 550 nm and λ_{peak} = 560 nm are lower and λ_{peak} = 570 is higher than for MDA-MB-468. This shift in the λ_{peak} distribution towards longer wavelengths is indicative of a NP sub-population with a red-shifted plasmon resonance. The most prominent changes in λ_{peak} associated with NP binding to the cell surface for both HeLa and MDA-MB-468 in **Figure 5A** and **B** occur in a relatively narrow spectral window between λ_{peak} = 540 - 580 nm. We calculated the intensity ratio $R = I_{570}/I_{540}$ of the 540 $\pm$ 5 nm and 570 $\pm$ 5 nm intensity channels for all NP pixels as a measure for electromagnetic coupling. The histogram in **Figure 5C** shows a progressively increasing red-shift (increase in R) relative to the NP controls (R_{av} = 1.22 and 1.23 respectively, for NPs before and after recovery) in the sequence MDA-MB-468 −EGF (R_{av} = 1.44), MDA-MB-468 +EGF (R_{av} = 1.49), HeLa −EGF (R_{av} = 1.84), and HeLa +EGF (R_{av} = 2.03), where R_{av} is the average R value of the distribution. The differences in R between the cells as well as between the cells and the NP controls are significant with p-values < 0.001 (unpaired two-sample *t*-test). The differences between the individual cell lines $(-/+)$ EGF are weaker than between the cell lines but still statistically significant with p-values < 0.001 (unpaired two-sample *t*-test). The R_{av} values provide a metric that can be compared with the effective cluster diameters determined by dSTORM. We determined a correlation

coefficient of -0.8454, confirming a strong negative correlation between *R* values and EGFR cluster size (**Figure S5**).

Overall, the spectral analysis in **Figure 5** confirms that NP binding to EGFR results in a spatial clustering of the labels with sufficiently small interparticle separation to induce significant spectral red-shifts. Our analysis reveals that a ratiometric analysis of the intensities at 570 and 540 nm is well suited to discern the spectral differences between the investigated conditions. In principle, changes in the ambient refractive index can also induce a spectral shift between cell-bound NPs and glass-bound NP controls. However, the refractive indices of glass (n = 1.52)[68] and the cell membrane (n = 1.46 – 1.60)[69,70] are similar and a refractive index difference alone is insufficient to account for the difference in R_{av} between HeLa and MDA-MB-468 (−/+) EGF.

Probing Changes in EGFR Clustering Induced by Dissolution of Cortical Actin Network.

EGFR is an actin binding protein and its distribution and clustering tendency can be influenced by the structural organization of the actin cytoskeleton.[71] To test the sensitivities of hyperspectral plasmon coupling microscopy and dSTORM for detecting

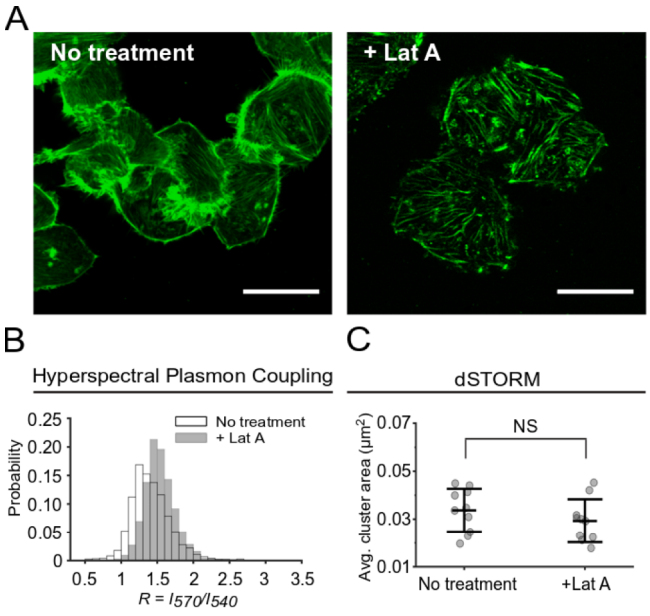

Figure 6: (A) Representative confocal images of untreated and 1 μM Lat A-treated MDA-MB-468 cells. Scale bar: 10 μm. **(B)** Histograms of $R = I_{570}/I_{540}$ for untreated and Lat A-treated MDA-MB-468 cells obtained from hyperspectral plasmon coupling microscopy. The presented data were collected from 50 cells (3 independent experiments). **(C)** Average cluster area for untreated and Lat A-treated MDA-MB-468 cells obtained from dSTORM. Each data point represents the average cluster area for two 4 μm × 4 μm regions per cell for a total of 10 cells each (3 independent experiments). Lines represent average ± SD. NS (not significant) by unpaired two-sample *t*-test.

potential differences in EGFR clustering after perturbation of the actin network**,** we pretreated MDA-MB-468 cells with Latrunculin A (Lat A), which sequesters free G-actin monomers and depolymerizes F-actin[72]. Confocal imaging of Lat A-treated cells in **Figure 6A** demonstrated the activity of the inhibitor while cells maintained their overall shape. **Figure 6B** summarizes the $R = I_{570}/I_{540}$ distributions for NP labels targeted at EGFR, as determined by hyperspectral plasmon coupling microscopy of samples without and with Lat A treatment. We observed a significant red-shift (increase in R) after Lat A treatment, with R_{av} (no treatment) = 1.44 and R_{av} (+Lat A) = 1.58 ($p < 0.001$, unpaired two-sample *t*-test). The detected increase in $R = I_{570}/I_{540}$ after actin perturbation indicates that the average interparticle separation in Lat A-treated cells are shorter, which suggests that the size of the EGFR clusters has decreased through Lat A treatment. Furthermore, fluorescence superresolution images acquired by dSTORM also show a trend of a small decrease in average cluster size from 0.034 ± 0.009 μm^2 to 0.029 ± 0.009 μm^2 after actin perturbation, but the change is statistically not significant for the relatively small sample size (10 cells) investigated. Analysis of individual clusters from the dSTORM binary maps revealed an average EGFR cluster size of 158 ± 95 nm after actin perturbation in MDA-MB-468 cells.

DISCUSSION

The dSTORM data confirm a heterogeneous spatial distribution of the cell surface EGFR in both MDA-MB-468 and HeLa cells with average cluster sizes of 172 ± 99 nm (−EGF) and 155 ± 91 nm (+EGF) in MDA-MB-468 and 150 ± 90 nm and 145 ± 90 nm, respectively, in HeLa. Our measurements of the average cluster size for HeLa (−/+) EGF is in agreement with a previous near-field scanning optical microscopy study[14], however, to the best of our knowledge, the average EGFR cluster size has not yet been reported

for MDA-MB-468 (−/+) EGF. The increase in the size of EGFR clusters in MDA-MB-468 when compared with HeLa is accompanied by a higher number of receptors per cluster. We determined on average 15 EGFR/cluster for MDA-MB-468 (−EGF) compared with 10 EGFR/cluster for HeLa.

The dSTORM results facilitate testing the sensitivity of hyperspectral plasmon coupling microscopy for differentiating between different EGFR cluster sizes. The resonance wavelength of gold NP labels with a diameter of 72.17 ± 2.16 nm targeted at EGFR exhibited significantly larger spectral shifts for HeLa than for MDA-MB-468 in the absence of EGF stimulation. The experimentally observed spectral shifts in the NP plasmon resonance can be rationalized in the context of the large-scale EGFR clustering determined by dSTORM. The size of the EGFR clusters in both cell lines is large enough to accommodate binding of multiple NPs of the chosen size, but, at the same time, small enough so that independently bound NP labels can be sufficiently close to facilitate electromagnetic coupling. Due to the strong distance-dependence of the near-field coupling, differences in the average separation between NPs associated with EGFR clusters with different physical footprints result in spectral shifts, which are observed as differences in R_{av} in **Figure 5C**. The spectral shift between NPs bound to cells and unbound NPs confirm NP clustering on the cell surface that results in electromagnetic coupling between the bound NP labels. Consistent with the dSTORM observation that EGFR clusters are smaller for HeLa than for MDA-MB-468, the spectra of the NP labels targeted to HeLa are red-shifted relative to those bound to MDA-MB-468. Shorter average interparticle separations as result of stronger spatial confinement accounts for the observed spectral shift. The increase in scattering intensity of the NP labels in the sequence, individual NP labels (controls) < NP bound to MDA-MB-468 –EGF < NP bound

to HeLa – EGF observed in **Figure 3C**, is also consistent with an increase in electromagnetic coupling in that sequence.

Our hyperspectral plasmon coupling measurements indicate that EGFR activation through addition of EGF results in smaller EGFR cluster sizes for both cell lines. This change in cluster size is detected as a small but significant red-shift in R_{av} for both cell lines upon growth factor addition. The change in EGFR cluster size after activation was more apparent and significant for MDA-MB-468, owing to the overexpression of EGFR, compared with HeLa. One point that deserves further discussion is the observation in **Figure 3C** that the overall scattering intensity of the NP labels after EGFR activation with free EGF decreases for both HeLa and MDA-MB-468, as shorter interparticle separations should further increase the near-field coupling and, thus, enhance the scattering cross-section. However, it is known that EGF binding to EGFR triggers endocytosis and we, consequently, attribute the reduced intensity to a loss of EGFR clusters in the membrane after EGF stimulation due to growth factor triggered endocytosis.[14]

The observed spatial heterogeneity of EGFR may be influenced by molecular and structural factors such as the actin cytoskeleton, which is considered an important factor for regulating clustering of EGFR[73] and other receptors[74–76] through compartmentalization of the plasma membrane. Our combined hyperspectral plasmon coupling and dSTORM analyses revealed that in the EGFR overexpressing MDA-MB-468 cell line, depolymerization of actin results in the formation of geometrically smaller clusters. After actin perturbation, the average EGFR cluster size decreases by 14 nm to 158 $\pm$ 95 nm, which is accompanied by a spectral red-shift of the plasmon resonance (**Figure 6B**). One possible explanation for this observation is that the receptor confinement induced by the cortical actin network increases inter-EGFR interactions of the co-confined receptors and, thus, favors the formation of EGFR clusters.[77] Depolymerization of actin by Lat A reduces

cluster confinement and, according to our data, leads to the formation of smaller clusters containing less EGFR per cluster (**Figure S6**) when compared with untreated MDA-MB-468 cells.

Although spectral imaging of plasmon coupling between NP labels does not allow for a direct quantification of EGFR cluster size, as in the case of dSTORM, our data confirm that the hyperspectral plasmon coupling microscopy approach can reliably detect differences and changes in EGFR cluster size. Considering the size of the NPs used in this work, it is clear that plasmon coupling microscopy is not as universally applicable as other superresolution microscopies that use smaller labels. However, for the application in this work, characterization of the large-scale clustering of EGFR, the chosen NP size made the plasmon coupling assay very sensitive to changes in EGFR clustering. In fact, the conclusions from the spectral shift analysis are in very good agreement with the dSTORM results. Both techniques differ, however, greatly in experimental throughput (**Figure 7**). In hyperspectral plasmon coupling microscopy we collected all the required information to quantify the spectra of the NPs bound to EGFR within 1.2 s. At 1.2 s for dSTORM, only 16 localizations have been localized leading to an incomplete and not useful cluster map.

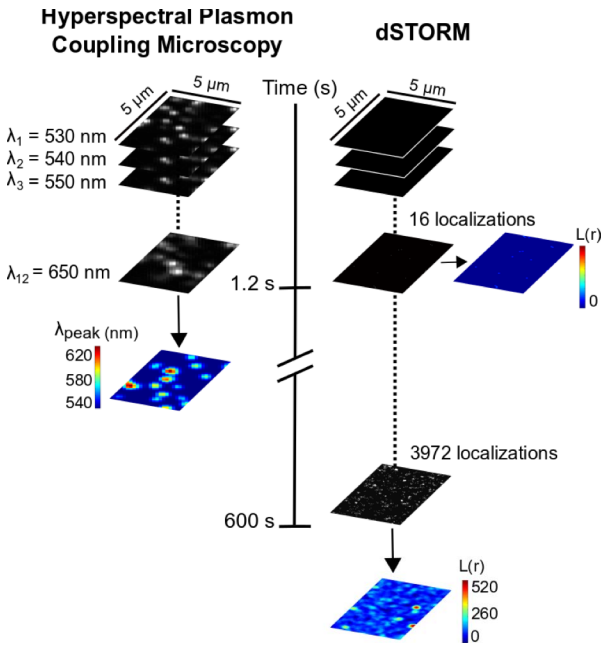

Figure 7. Comparison of hyperspectral plasmon coupling microscopy and dSTORM applied for optical mapping of NP labels and fluorescence labeling of EGFR on independent 5 µm × 5 µm area of HeLa cell, respectively. At the same acquisition time of 0.1 s per frame, the cluster map of peak resonance wavelength for hyperspectral imaging is complete in 1.2 s, while for dSTORM, only 16 localizations have been localized leading to an incomplete cluster map. A complete cluster map for dSTORM requires thousands of frames for sufficient localizations (approximately 600 s).

To obtain sufficient localizations to reconstruct a dSTORM image, we needed to record at least 10,000 frames over a total acquisition time of 600 s (**Figure S7**). Importantly, in the time it takes to record 10,000 frames in dSTORM for 1 field of view, we can acquire data for roughly 500 field of views using hyperspectral plasmon coupling microscopy, which underlines the great advantage in scalability for this approach. For important sensing and screening applications, the ability to detect relative changes in receptor clustering for a large number of individual cells in a relatively short time may outweigh the advantages provided by precise localization of individual receptor molecules in a cluster.

CONCLUSION

We applied both hyperspectral plasmon coupling microscopy and fluorescence superresolution dSTORM microscopy to investigate EGFR clustering in MDA-MB-468 and HeLa cells. Our comparative studies suggest that a systematic spectral analysis of the distance-dependent plasmon coupling between NP facilitates a sensitive detection of differences in the size of EGFR clusters in both cell lines as well as changes induced by addition of EGF or dissolution of the cortical actin network as indicated by the dSTORM data. The successful distinction of changes in clustering patterns under different experimental conditions using bright and easy to image NP labels emphasizes the potential of this approach for achieving a rapid characterization of receptor clustering in a large cell population with single cell resolution in a conventional widefield microscope. Spatial clustering of EGFR warrants increased interaction frequencies between EGFR (and co-receptors) and favors their association into dimers[5,9] and higher oligomers[6,7,78]. Given the role of EGFR oligomerization in enhancing receptor phosphorylation, receptor clustering could be a regulation mechanism to control and modulate ligand binding induced receptor signaling.[17–19] The putative regulatory role of receptor clustering creates

a need for tools that can characterize receptor clustering with adequate throughput. This work confirms hyperspectral plasmon coupling microscopy of NP labels as a scalable analytical tool for surveying the spatial clustering of receptors in the plasma membrane. Through automation of the image acquisition procedure, the approach could provide a useful assay for receptor clustering (and its heterogeneity) to complement existing techniques for the quantification of expression levels of a cell surface receptor in a cell population, such as flow cytometry. The NP-based imaging tool paves a path towards including large-scale receptor clustering on the single cell level as a biomarker in the characterization of heterogeneous cell populations.

Acknowledgement

This work was supported by the National Science Foundation (NSF) through grant 1808241 and the National Institutes of Health (NIH) through grant R01CA138509.

Supporting Information

Localization precision and spatial resolution of dSTORM images, Hydrodynamic diameter and UV-Vis spectra of NP labels, Hopkins Statistics of digital color images, Hopkins Statistics of SEM images, Correlation plot of R_{av} and average EGFR cluster size, EGFR/cluster for Lat A-treated samples from dSTORM, number of frames for dSTORM image reconstruction, dSTORM drift correction, specificity and selectivity of NP labels targeted to EGFR.

METHODS

Cell Culture and Treatments. MDA-MB-468 cells were cultured in Advanced Dulbecco's Modified Eagle Medium (DMEM) supplemented with 10% fetal bovine serum, L-glutamine,

penicillin, and streptomycin at 37°C with a humidified atmosphere containing 5% CO_2. HeLa cells were cultured under the same conditions. Prior to experiments, MDA-MB-468 and HeLa cells were maintained in serum-free DMEM for 16 h. Cells to be imaged under dSTORM and hyperspectral plasmon coupling microscopy were cultured in glass bottom petri dishes to approximately 80% confluency for experiments. EGF-stimulated cell samples were serum-starved for 16 h and incubated with 10 nM EGF (ThermoFisher Scientific) for 10 min at 37°C before washing and fixation with 4% paraformaldehyde. Cell samples in which actin was depolymerized were serum-starved for 16 h and incubated with 1 μM of Latrunculin A (Sigma-Aldrich) for 10 min at 37°C before washing and fixation with 4% paraformaldehyde.

dSTORM Sample Preparation. Cells were immunostained after fixation with an Alexa-Fluor 647-conjugated antibody against EGFR (0.5 μg/mL, ThermoFisher Scientific) in the dark for 20 min and then washed three times with 1× PBS for 5 min each. For dSTORM imaging, the oxygen-scavenging buffer (50 mM TRIS and 10 mM NaCl solution to pH 8) contained 0.5 mg/mL glucose oxidase, 40 μg/mL catalase, 10% glucose (m/v), and 10 mM mercaptoethylamine (MEA). The buffer solution was added to the glass bottom petri dish prior to imaging.

dSTORM Imaging. For imaging, a 642-nm laser and an electron-multiplying charge-coupled device were used (Andor iXonEM+ 897 back-illuminated EMCCD). dSTORM imaging was performed on a Zeiss ELYRA PS.1 microscope using an alpha Plan-Apochromat 100× oil objective with NA 1.46. Samples were imaged in TIRF illumination mode with the TIRF angle adjusted to ensure that the focal plane was on the apical surface of the cells.[79] A total of 10,000 raw images were acquired per cell with an exposure time

of 50 ms for the reconstruction of superresolution images. One single reconstructed dSTORM image was acquired in less than 10 mins. Single molecule localizations were fitted to a 2D Gaussian using the Zeiss Zen Black software that was equipped with the imaging system to obtain histograms of localization precision. The spatial resolution was estimated by Fourier Ring Correlation (FRC) analysis[80] using SharpVisu[81] software on MATLAB.

dSTORM Data Analysis. dSTORM images were reconstructed from raw image TIFF stacks with the ImageJ plug-in QuickPALM[82]. For each frame, localizations corresponding to single emission events were identified with a minimum SNR of 2. The x-y drift was corrected post-acquisition using a cross-correlation method via SharpViSu[81] software on MATLAB (**Figure S8**). The drift-corrected x-y coordinates were imported into ClusterVisu[81] MATLAB software for further quantitative cluster analysis as described by Owen et al[83,84]. Avoiding cell edges, two non-overlapping regions of 4 × 4 μm^2 were selected per cell for quantitative cluster analysis in reconstructed images. To analyze the spatial distribution of molecules, Ripley's *K*-function was calculated using ClusterViSu as shown in Eqn. 1:

$$K(r) = A\sum_{i=1}^{n}\sum_{j=1}^{n}\left(\frac{\delta_{ij}}{n^2}\right) \text{ where } \delta_{ij} = 1 \text{ if } \delta_{ij} < r, \text{otherwise } 0 \qquad (1)$$

where *K(r)* is the *K*-function, *A* is the area of the region being analyzed, *n* is the total number of localizations within that area, δ_{ij} is the distance between points i and j, and *r* is the spatial scale. In this analysis, concentric circles of radius *r* is drawn around each localization and counts how many other localizations are encircled and compared to a random distribution. The *K*-function can be normalized to scale with radius, which yields the *H*-and *L*-function as shown in Eqn. 2:

$$H(r) = \sqrt{K(r)/\pi} - r \; = \; L(r) - r \qquad (2)$$

For a spatially random distribution of localizations, *L(r)-r* = 0 for all *r*. For clustered localizations, this value is positive. The cluster map was generated by interpolating a surface plot with *L(r)* for *r* = 80 nm of every localization as the z-axis and shown using a pseudo-color scale. Then the cluster map was thresholded by an *L(r)* cut-off value of 120-130 to best define clusters to generate a binary map which contained quantitative information about the clusters. To estimate the number of EGFR/cluster, the number of localizations in a cluster was divided by 7.8, which is the ratio of Alexa 647 dye conjugated to a single anti-EGFR antibody.

Liposome and Particle Preparation. Lipid-wrapped NPs were prepared as described previously.[63–65] The liposome mixture contained 55 mol % 1,2-dipalmitoyl-*sn*-glycero-3-phosphocholine (DPPC), 2 mol % 1,2-dioleoyl-*sn*-glycero-3- phospho-L-serine (DOPS), 4 mol % of 1,2-distearoyl-*sn*-glycero-3-phosphoethanolamine-N-[biotinyl(polyethylene glycol)-2000] (DSPE-PEG(2000)-Biotin), and 39 mol % cholesterol in chloroform. This lipid mixture was tethered to the NP via octadecanethiol by incubating for 17 h on a rocker. The lipid-wrapped NPs were subsequently dialyzed overnight in Milli-Q water with nuclepore track-etched membranes (Whatman, pore size 0.015 μm). After dialysis, the NPs were centrifuged once (3.4k rpm, 10 min) to obtain the NP pellet. For cell experiments, this pellet was resuspended in 0.1× PBS to make a 150 pM NP solution.

Immunolabeling. To functionalize the anti-EGFR antibody (Sigma-Aldrich, clone 102618), 4 μL of biotin N-hydroxysuccinimide ester (100 mg/mL in DMSO) was mixed with 200 μL of 100 μg/mL anti-EGFR antibody solution (1× PBS, pH 7.2) and kept in an ice

bath for 6 h. Excess biotin NHS ester was removed using a size exclusion Zeba column (7K MWCO). The functionalized antibody can be stored at −20°C until further use. For labeling, cells were briefly rinsed with prewarmed 1× HBSS buffer and then fixed by immersion in 4% paraformaldehyde for 10 min at room temperature, followed by three washes with 1× PBS for 5 min each. Subsequently, the cells were incubated in 1× PBS buffer containing 1% BSA for 30 min at room temperature to block nonspecific binding. Cells were then washed three times with ice-cold 1× PBS for 5 min each and then incubated with biotin-functionalized anti-EGFR antibody (diluted 1:10 in 1 × PBS) overnight at 4°C. The cells were then washed three times with 1× PBS for 5 min each and incubated with 0.1 mg/mL of NeutrAvidin for 30 min at room temperature. After that, the cells were washed three times with ice-cold 1× PBS for 5 min each, except with 0.1× PBS for the last wash. In the subsequent immunolabeling step, the petri dish was covered with 300 μL of 150 pM of lipid-wrapped NPs in 0.1× PBS for 30 min at 4°C and then washed three times with 0.1× PBS for 5 min each. The glass bottom petri dishes can then be transferred to a darkfield microscope for hyperspectral plasmon coupling microscopy. We validated in a control experiment that the binding of NP labels to EGFR was specific and selective (**Figure S9**).

Hyperspectral Plasmon Coupling Microscopy. All optical imaging experiments were performed with an Olympus IX71 inverted microscope. For whitelight dark-field imaging, the samples were illuminated with a 100 W tungsten lamp through a high NA oil condenser (NA = 1.2-1.4) and the scattered light was collected through a 60× oil objective (NA = 0.65). Digital color images were collected under whitelight illumination with a Nikon D5100 DSLR digital camera connected to the microscope through an eyepiece adapter. For hyperspectral imaging, a VariSpec-liquid crystal tunable filter was added in front of the

darkfield condenser and used to tune the excitation wavelength. Hyperspectral images were captured with an electron multiplying CCD (Andor, Ixon^{+}). A monochromatic image was obtained from 540-650 nm, every 10 nm, for a total of 12 images. The exposure time for each image was 0.1 s and the acquisition time for a full set of 12 images was 1.2 s. The spatial resolution was determined by fitting the point spread function (PSF) of randomly selected NP emitters with a 2D Gaussian and determining the full width at half max (FWHM) of the fit. For the localization precision, the Andor software was operated in photon counting mode to acquire images of NPs immobilized on glass. Random NPs were selected and fitted with a 2D Gaussian to obtain the number of detected photons. The localization precision was calculated as described by Ober et al[85].

Hyperspectral Image Processing. All image processing was performed using custom-written MATLAB codes. Monochromatic images were corrected for the background and excitation profile. We focused in our analysis on the central region of the cells (peripheral regions were excluded) and included only pixels whose total intensity was at least one standard deviation above the average cell background over the entire wavelength range. For λ_{peak} histograms, the intensity of the wavelength channel with the highest NP intensity was set to 1 and all others 0 for each pixel. For $R = I_{570}/I_{540}$ histograms, the ratio of NP intensities on the 570 nm and 540 nm channel were divided for every pixel. The mean intensity of NPs were determined using the particle picker plugin on ImageJ.

SEM Sample Preparation and Imaging. The culturing and immunolabeling procedures were identical to the sample preparation for hyperspectral plasmon coupling microscopy except the cells were plated on a 1 × 1 cm silicon substrate. After fixation and

immunolabeling, the silicon substrates containing NP labeled cells were washed three times with ice-cold 0.1× PBS and then briefly immersed in Milli-Q water to remove any remaining salt on the surface. The substrate was then gently blow-dried in a nitrogen stream and left overnight in a vacuum desiccator. The samples were imaged using Zeiss Supra40VP at 5.0 kV and a working distance of 8 mm.

REFERENCES

(1) Roskoski, R., J. The ErbB/HER Family of Protein-Tyrosine Kinases and Cancer. *Pharmacol Res* **2014**, *79*, 34–74.

(2) Zhang, X.; Gureasko, J.; Shen, K.; Cole, P. A.; Kuriyan, J. An Allosteric Mechanism for Activation of the Kinase Domain of Epidermal Growth Factor Receptor. *Cell* **2006**, *125* (6), 1137–1149.

(3) Lemmon, M. A.; Schlessinger, J. Cell Signaling by Receptor Tyrosine Kinases. *Cell* **2010**, *141* (7), 1117–1134.

(4) Yarden, Y.; Schlessinger, J. Self-Phosphorylation of Epidermal Growth Factor Receptor: Evidence for a Model of Intermolecular Allosteric Activation. *Biochemistry* **1987**, *26* (5), 1434–1442.

(5) Schlessinger, J. Ligand-Induced, Receptor-Mediated Dimerization and Activation of EGF Receptor. *Cell*. 2002, pp 669–672.

(6) Clayton, A. H. A.; Walker, F.; Orchard, S. G.; Henderson, C.; Fuchs, D.; Rothacker, J.; Nice, E. C.; Burgess, A. W. Ligand-Induced Dimer-Tetramer Transition during the Activation of the Cell Surface Epidermal Growth Factor Receptor-A Multidimensional Microscopy Analysis. *J. Biol. Chem.* **2005**, *280* (34), 30392–30399.

(7) Clayton, A. H. A.; Orchard, S. G.; Nice, E. C.; Posner, R. G.; Burgess, A. W.

Predominance of Activated EGFR Higher-Order Oligomers on the Cell Surface. *Growth Factors* **2008**, *26* (6), 316–324.

(8) van Lengerich B, Agnew C, Puchner EM, Huang B, J. N. EGF and NRG Induce Phosphorylation of HER3/ERBB3 by EGFR Using Distinct Oligomeric Mechanisms. *Proc. Natl. Acad. Sci.* **2017**, *114* (14), E2836–E2845.

(9) Chung, I.; Akita, R.; Vandlen, R.; Toomre, D.; Schlessinger, J.; Mellman, I. Spatial Control of EGF Receptor Activation by Reversible Dimerization on Living Cells. *Nature* **2010**, *464* (7289), 783–787.

(10) Huang, Y.; Bharill, S.; Karandur, D.; Peterson, S. M.; Marita, M.; Shi, X.; Kaliszewski, M. J.; Smith, A. W.; Isacoff, E. Y.; Kuriyan, J. Molecular Basis for Multimerization in the Activation of the Epidermal Growth Factor Receptor. *Elife* **2016**, *5*.

(11) Keating, E.; Nohe, A.; Petersen, N. O. Studies of Distribution, Location and Dynamic Properties of EGFR on the Cell Surface Measured by Image Correlation Spectroscopy. *Eur. Biophys. J.* **2008**, *37* (4), 469–481.

(12) Webb, S. E. D.; Roberts, S. K.; Needham, S. R.; Tynan, C. J.; Rolfe, D. J.; Winn, M. D.; Clarke, D. T.; Barraclough, R.; Martin-Fernandez, M. L. Single-Molecule Imaging and Fluorescence Lifetime Imaging Microscopy Show Different Structures for High- and Low-Affinity Epidermal Growth Factor Receptors in A431 Cells. *Biophys. J.* **2008**, *94* (3), 803–819.

(13) Szabó, Á.; Horváth, G.; Szöllosi, J.; Nagy, P. Quantitative Characterization of the Large-Scale Association of ErbB1 and ErbB2 by Flow Cytometric Homo-FRET Measurements. *Biophys. J.* **2008**, *95* (4), 2086–2096.

(14) Abulrob, A.; Lu, Z.; Baumann, E.; Vobornik, D.; Taylor, R.; Stanimirovic, D.; Johnston, L. J. Nanoscale Imaging of Epidermal Growth Factor Receptor

Clustering. *J. Biol. Chem.* **2009**, *285* (5), 3145–3156.

(15) Sieber, J. J.; Willig, K. I.; Kutzner, C.; Gerding-Reimers, C.; Harke, B.; Donnert, G.; Rammner, B.; Eggeling, C.; Hell, S. W.; Grubmüller, H.; et al. Anatomy and Dynamics of a Supramolecular Membrane Protein Cluster. *Science (80-.).* **2007**, *317* (5841), 1072–1076.

(16) Kusumi, A.; Nakada, C.; Ritchie, K.; Murase, K.; Suzuki, K.; Murakoshi, H.; Kasai, R. S.; Kondo, J.; Fujiwara, T. Paradigm Shift of the Plasma Membrane Concept from the Two-Dimensional Continuum Fluid to the Partitioned Fluid: High-Speed Single-Molecule Tracking of Membrane Molecules. *Annu. Rev. Biophys. Biomol. Struct.* **2005**, *34* (1), 351–378.

(17) Ichinose, J.; Murata, M.; Yanagida, T.; Sako, Y. EGF Signalling Amplification Induced by Dynamic Clustering of EGFR. *Biochem. Biophys. Res. Commun.* **2004**, *324* (3), 1143–1149.

(18) Bray, D.; Levin, M. D.; Morton-Firth, C. J. Receptor Clustering as a Cellular Mechanism to Control Sensitivity. *Nature* **1998**, *393* (6680), 85–88.

(19) Bethani, I.; Skånland, S. S.; Dikic, I.; Acker-Palmer, A. Spatial Organization of Transmembrane Receptor Signalling. *EMBO Journal*. 2010, pp 2677–2688.

(20) Caré, B. R.; Soula, H. A. Impact of Receptor Clustering on Ligand Binding. *BMC Syst. Biol.* **2011**, *5*.

(21) Caré, B. R.; Soula, H. A. Receptor Clustering Affects Signal Transduction at the Membrane Level in the Reaction-Limited Regime. *Phys. Rev. E - Stat. Nonlinear, Soft Matter Phys.* **2013**, *87* (1).

(22) Stabley, D.; Retterer, S.; Marshall, S.; Salaita, K. Manipulating the Lateral Diffusion of Surface-Anchored EGF Demonstrates That Receptor Clustering Modulates Phosphorylation Levels. *Integr. Biol. (United Kingdom)* **2013**, *5* (4),

659–668.

(23) Kozer, N.; Barua, D.; Orchard, S.; Nice, E. C.; Burgess, A. W.; Hlavacek, W. S.; Clayton, A. H. A. Exploring Higher-Order EGFR Oligomerisation and Phosphorylation - A Combined Experimental and Theoretical Approach. *Mol. Biosyst.* **2013**, *9* (7), 1849–1863.

(24) Valley, C. C.; Lidke, K. A.; Lidke, D. S. The Spatiotemporal Organization of ErbB Receptors: Insights from Microscopy. *Cold Spring Harb. Perspect. Biol.* **2014**, *6* (2).

(25) Boyd, P. S.; Struve, N.; Bach, M.; Eberle, J. P.; Gote, M.; Schock, F.; Cremer, C.; Kriegs, M.; Hausmann, M. Clustered Localization of EGFRvIII in Glioblastoma Cells as Detected by High Precision Localization Microscopy. *Nanoscale* **2016**, *8* (48), 20037–20047.

(26) Saffarian, S.; Li, Y.; Elson, E. L.; Pikey, L. J. Oligomerization of the EGF Receptor Investigated by Live Cell Fluorescence Intensity Distribution Analysis. *Biophys. J.* **2007**, *93* (3), 1021–1031.

(27) Nagy, P.; Claus, J.; Jovin, T. M.; Arndt-Jovin, D. J. Distribution of Resting and Ligand-Bound ErbB1 and ErbB2 Receptor Tyrosine Kinases in Living Cells Using Number and Brightness Analysis. *Proc. Natl. Acad. Sci.* **2010**, *107* (38), 16524–16529.

(28) Ibach, J.; Radon, Y.; Gelléri, M.; Sonntag, M. H.; Brunsveld, L.; Bastiaens, P. I. H.; Verveer, P. J. Single Particle Tracking Reveals That EGFR Signaling Activity Is Amplified in Clathrin-Coated Pits. *PLoS One* **2015**, *10* (11).

(29) Sergé, A.; Bertaux, N.; Rigneault, H.; Marguet, D. Dynamic Multiple-Target Tracing to Probe Spatiotemporal Cartography of Cell Membranes. *Nat. Methods* **2008**, *5* (8), 687–694.

(30) Lidke, D. S.; Nagy, P.; Heintzmann, R.; Arndt-Jovin, D. J.; Post, J. N.; Grecco, H. E.; Jares-Erijman, E. A.; Jovin, T. M. Quantum Dot Ligands Provide New Insights into ErbB/HER Receptor-Mediated Signal Transduction. *Nat. Biotechnol.* **2004**, *22* (2), 198–203.

(31) Wang, Y.; Gao, J.; Guo, X.; Tong, T.; Shi, X.; Li, L.; Qi, M.; Wang, Y.; Cai, M.; Jiang, J.; et al. Regulation of EGFR Nanocluster Formation by Ionic Protein-Lipid Interaction. *Cell Res.* **2014**, *24* (8), 959–976.

(32) Gao, J.; Wang, Y.; Cai, M.; Pan, Y.; Xu, H.; Jiang, J.; Ji, H.; Wang, H. Mechanistic Insights into EGFR Membrane Clustering Revealed by Super-Resolution Imaging. *Nanoscale* **2015**, *7* (6), 2511–2519.

(33) Zhang, R.; Fruhwirth, G. O.; Coban, O.; Barrett, J. E.; Burgoyne, T.; Lee, S. H.; Simonson, P. D.; Baday, M.; Kholodenko, B. N.; Futter, C. E.; et al. Probing the Heterogeneity of Protein Kinase Activation in Cells by Super-Resolution Microscopy. *ACS Nano* **2017**, *11* (1), 249–257.

(34) Godin, A. G.; Lounis, B.; Cognet, L. Super-Resolution Microscopy Approaches for Live Cell Imaging. *Biophysical Journal*. 2014, pp 1777–1784.

(35) Nahidiazar, L.; Agronskaia, A. V.; Broertjes, J.; Van Broek, B. Den; Jalink, K. Optimizing Imaging Conditions for Demanding Multi-Color Super Resolution Localization Microscopy. *PLoS One* **2016**, *11* (7).

(36) Glushonkov, O.; Réal, E.; Boutant, E.; Mély, Y.; Didier, P. Optimized Protocol for Combined PALM-DSTORM Imaging. *Sci. Rep.* **2018**, *8* (1).

(37) Sengupta, P.; van Engelenburg, S. B.; Lippincott-Schwartz, J. Superresolution Imaging of Biological Systems Using Photoactivated Localization Microscopy. *Chem. Rev.* **2014**, *114* (6), 3189–3202.

(38) Crow, M. J.; Seekell, K.; Ostrander, J. H.; Wax, A. Monitoring of Receptor

Dimerization Using Plasmonic Coupling of Gold Nanoparticles. *ACS Nano* **2011**, *5* (11), 8532–8540.

(39) Rong, G.; Wang, H.; Skewis, L. R.; Reinhard, B. M. Resolving Sub-Diffraction Limit Encounters in Nanoparticle Tracking Using Live Cell Plasmon Coupling Microscopy. *Nano Lett.* **2008**, *8* (10), 3386–3393.

(40) Wang, J.; Yu, X.; Boriskina, S. V.; Reinhard, B. M. Quantification of Differential ErbB1 and ErbB2 Cell Surface Expression and Spatial Nanoclustering through Plasmon Coupling. *Nano Lett.* **2012**, *12* (6), 3231–3237.

(41) Wang, J.; Boriskina, S. V.; Wang, H.; Reinhard, B. M. Illuminating Epidermal Growth Factor Receptor Densities on Filopodia through Plasmon Coupling. *ACS Nano* **2011**, *5* (8), 6619–6628.

(42) Yu, X.; Wang, J.; Feizpour, A.; Reinhard, B. M. Illuminating the Lateral Organization of Cell-Surface CD24 and CD44 through Plasmon Coupling between Au Nanoparticle Immunolabels. *Anal. Chem.* **2013**, *85* (3), 1290–1294.

(43) Wang, H.; Wu, L.; Reinhard, B. M. Scavenger Receptor Mediated Endocytosis of Silver Nanoparticles into J774A.1 Macrophages Is Heterogeneous. *ACS Nano* **2012**, *6* (8), 7122–7132.

(44) Zhang, Q.; Reinhard, B. M. Ligand Density and Nanoparticle Clustering Cooperate in the Multivalent Amplification of Epidermal Growth Factor Receptor Activation. *ACS Nano*. 2018.

(45) Kreibig, U. & Vollmer, M. *Optical Properties of Metal Clusters*; Springer, 1995.

(46) Hu, Q.; Tay, L. L.; Noestheden, M.; Pezacki, J. P. Mammalian Cell Surface Imaging with Nitrile-Functionalized Nanoprobes: Biophysical Characterization of Aggregation and Polarization Anisotropy in SERS Imaging. *J. Am. Chem. Soc.* **2007**, *129* (1), 14–15.

(47) Kennedy, D. C.; Tay, L. L.; Lyn, R. K.; Rouleau, Y.; Hulse, J.; Pezacki, J. P. Nanoscale Aggregation of Cellular B2-Adrenergic Receptors Measured by Plasmonic Interactions of Functionalized Nanoparticles. *ACS Nano* **2009**, *3* (8), 2329–2339.

(48) Chung, T.; Koker, T.; Pinaud, F. Split-GFP: SERS Enhancers in Plasmonic Nanocluster Probes. *Small* **2016**, *12* (42), 5891–5901.

(49) Wu, L.; Reinhard, B. M. Probing Subdiffraction Limit Separations with Plasmon Coupling Microscopy: Concepts and Applications. *Chemical Society Reviews*. 2014, pp 3884–3897.

(50) Crow, M. J.; Grant, G.; Provenzale, J. M.; Wax, A. Molecular Imaging and Quantitative Measurement of Epidermal Growth Factor Receptor Expression in Live Cancer Cells Using Immunolabeled Gold Nanoparticles. *Am. J. Roentgenol.* **2009**, *192* (4), 1021–1028.

(51) Aaron, J.; Nitin, N.; Travis, K.; Kumar, S.; Collier, T.; Park, S. Y.; José-Yacamán, M.; Coghlan, L.; Follen, M.; Richards-Kortum, R.; et al. Plasmon Resonance Coupling of Metal Nanoparticles for Molecular Imaging of Carcinogenesis in Vivo. *J. Biomed. Opt.* **2007**, *12* (3), 034007.

(52) Aaron, J.; Travis, K.; Harrison, N.; Sokolov, K. Dynamic Imaging of Molecular Assemblies in Live Cells Based on Nanoparticle Plasmon Resonance Coupling. *Nano Lett.* **2009**, *9* (10), 3612–3618.

(53) Berkers, J. A. M.; Van Bergen En Henegouwen, P. M. P.; Boonstra, J. THE JOURNAL OF BIOLOGICAL CHEMISTRY Three Classes of Epidermal Growth Factor Receptors on HeLa Cells*. *J. Biol. Chem.* **1991**, *266* (2), 922–927.

(54) Filmus, J.; Pollak, M. N.; Cailleau, R.; Buick, R. N. MDA-468, a Human Breast Cancer Cell Line with a High Number of Epidermal Growth Factor (EGF)

Receptors, Has an Amplified EGF Receptor Gene and Is Growth Inhibited by EGF. *Biochem. Biophys. Res. Commun.* **1985**, *128* (2), 898–905.

(55) Su, K. H.; Wei, Q. H.; Zhang, X.; Mock, J. J.; Smith, D. R.; Schultz, S. Interparticle Coupling Effects on Plasmon Resonances of Nanogold Particles. *Nano Lett.* **2003**, *3* (8), 1087–1090.

(56) Rechberger, W.; Hohenau, A.; Leitner, A.; Krenn, J. R.; Lamprecht, B.; Aussenegg, F. R. Optical Properties of Two Interacting Gold Nanoparticles. *Opt. Commun.* **2003**, *220* (1–3), 137–141.

(57) Reinhard, B. M.; Siu, M.; Agarwal, H.; Alivisatos, A. P.; Liphardt, J. Calibration of Dynamic Molecular Rulers Based on Plasmon Coupling between Gold Nanoparticles. *Nano Lett.* **2005**, *5* (11), 2246–2252.

(58) Yang, L.; Wang, H.; Yan, B.; Reinhard, B. M. Calibration of Silver Plasmon Rulers in the 1-25 Nm Separation Range: Experimental Indications of Distinct Plasmon Coupling Regimes. *J. Phys. Chem. C* **2010**, *114* (11), 4901–4908.

(59) Lerch, S.; Reinhard, B. M. Quantum Plasmonics: Optical Monitoring of DNA-Mediated Charge Transfer in Plasmon Rulers. *Adv. Mater.* **2016**, *28* (10), 2030–2036.

(60) Prodan, E.; Radloff, C.; Halas, N. J.; Nordlander, P. A Hybridization Model for the Plasmon Response of Complex Nanostructures. *Science (80-.).* **2003**, *302* (5644), 419–422.

(61) Nordlander, P.; Oubre, C.; Prodan, E.; Li, K.; Stockman, M. I. Plasmon Hybridization in Nanoparticle Dimers. *Nano Lett.* **2004**, *4* (5), 899–903.

(62) Yguerabide, J.; Yguerabide, E. E. Light-Scattering Submicroscopic Particles as Highly Fluorescent Analogs and Their Use as Tracer Labels in Clinical and Biological Applications II. Experimental Characterization. *Anal. Biochem.* **1998**,

262 (2), 157–176.

(63) Yu, X.; Feizpour, A.; Ramirez, N. G. P.; Wu, L.; Akiyama, H.; Xu, F.; Gummuluru, S.; Reinhard, B. M. Glycosphingolipid-Functionalized Nanoparticles Recapitulate CD169-Dependent HIV-1 Uptake and Trafficking in Dendritic Cells. *Nat. Commun.* **2014**, *5*.

(64) Yu, X.; Xu, F.; Ramirez, N. G. P.; Kijewski, S. D. G.; Akiyama, H.; Gummuluru, S.; Reinhard, B. M. Dressing up Nanoparticles: A Membrane Wrap to Induce Formation of the Virological Synapse. *ACS Nano* **2015**, *9* (4), 4182–4192.

(65) Yang, J. A.; Murphy, C. J. Evidence for Patchy Lipid Layers on Gold Nanoparticle Surfaces. *Langmuir* **2012**, *28* (12), 5404–5416.

(66) Uyemura, T.; Takagi, H.; Yanagida, T.; Sako, Y. Single-Molecule Analysis of Epidermal Growth Factor Signaling That Leads to Ultrasensitive Calcium Response. *Biophys. J.* **2005**, *88* (5), 3720–3730.

(67) Banerjee, A. & Dave, R. N. Validating Clusters Using the Hopkins Statistic. In *IEEE International Conference on Fuzzy Systems*; IEEE: Budapest,Hungary, 2004.

(68) Moh, K. J.; Yuan, X.-C.; Bu, J.; Zhu, S. W.; Gao, B. Z. Surface Plasmon Resonance Imaging of Cell-Substrate Contacts with Radially Polarized Beams. *Opt. Express* **2008**, *16* (25), 20734.

(69) Beuthan, J.; Minet, O.; Helfmann, J.; Herrig, M.; Müller, G. The Spatial Variation of the Refractive Index in Biological Cells. *Phys. Med. Biol.* **1996**, *41* (3), 369–382.

(70) Johnsen, S.; Widder, E. A. The Physical Basis of Transparency in Biological Tissue: Ultrastructure and the Minimization of Light Scattering. *J. Theor. Biol.* **1999**, *199* (2), 181–198.

(71) Den Hartigh, J. C.; Van Bergen En Henegouwen, P. M. P.; Verkleij, A. J.;

Boonstra, J. The EGF Receptor Is an Actin-Binding Protein. *J. Cell Biol.* **1992**, *119* (2), 349–355.

(72) Coué, M.; Brenner, S. L.; Spector, I.; Korn, E. D. Inhibition of Actin Polymerization by Latrunculin A. *FEBS Lett.* **1987**, *213* (2), 316–318.

(73) Boggara, M.; Athmakuri, K.; Srivastava, S.; Cole, R.; Kane, R. S. Characterization of the Diffusion of Epidermal Growth Factor Receptor Clusters by Single Particle Tracking. *Biochim. Biophys. Acta - Biomembr.* **2013**, *1828* (2), 419–426.

(74) Heasman, S. J.; Ridley, A. J. Mammalian Rho GTPases: New Insights into Their Functions from in Vivo Studies. *Nature Reviews Molecular Cell Biology*. 2008, pp 690–701.

(75) Charrier, C.; Ehrensperger, M.-V.; Dahan, M.; Levi, S.; Triller, A. Cytoskeleton Regulation of Glycine Receptor Number at Synapses and Diffusion in the Plasma Membrane. *J. Neurosci.* **2006**, *26* (33), 8502–8511.

(76) Wheeler, D.; Sneddon, W. B.; Wang, B.; Friedman, P. A.; Romero, G. NHERF-1 and the Cytoskeleton Regulate the Traffic and Membrane Dynamics of G Protein-Coupled Receptors. *J. Biol. Chem.* **2007**, *282* (34), 25076–25087.

(77) Fujiwara, T. K.; Iwasawa, K.; Kalay, Z.; Tsunoyama, T. A.; Watanabe, Y.; Umemura, Y. M.; Murakoshi, H.; Suzuki, K. G. N.; Nemoto, Y. L.; Morone, N.; et al. Confined Diffusion of Transmembrane Proteins and Lipids Induced by the Same Actin Meshwork Lining the Plasma Membrane. *Mol. Biol. Cell* **2016**, *27* (7), 1101–1119.

(78) Clayton, A. H. A.; Tavarnesi, M. L.; Johns, T. G. Unligated Epidermal Growth Factor Receptor Forms Higher Order Oligomers within Microclusters on A431 Cells That Are Sensitive to Tyrosine Kinase Inhibitor Binding. *Biochemistry* **2007**, *46* (15), 4589–4597.

(79) Teramura, Y.; Ichinose, J.; Takagi, H.; Nishida, K.; Yanagida, T.; Sako, Y. Single-Molecule Analysis of Epidermal Growth Factor Binding on the Surface of Living Cells. *EMBO J.* **2006**, *25* (18), 4215–4222.

(80) Nieuwenhuizen, R. P. J.; Lidke, K. A.; Bates, M.; Puig, D. L.; Grünwald, D.; Stallinga, S.; Rieger, B. Measuring Image Resolution in Optical Nanoscopy. *Nat. Methods* **2013**.

(81) Andronov, L.; Orlov, I.; Lutz, Y.; Vonesch, J. L.; Klaholz, B. P. ClusterViSu, a Method for Clustering of Protein Complexes by Voronoi Tessellation in Super-Resolution Microscopy. *Sci. Rep.* **2016**, *6*.

(82) Henriques, R.; Lelek, M.; Fornasiero, E. F.; Valtorta, F.; Zimmer, C.; Mhlanga, M. M. QuickPALM: 3D Real-Time Photoactivation Nanoscopy Image Processing in ImageJ. *Nat. Methods* **2010**, *7* (5), 339–340.

(83) Owen, D. M.; Williamson, D.; Magenau, A.; Gaus, K. Optical Techniques for Imaging Membrane Domains in Live Cells (Live-Cell Palm of Protein Clustering). *Methods Enzymol.* **2012**, *504*, 221–235.

(84) Owen, D. M.; Rentero, C.; Rossy, J.; Magenau, A.; Williamson, D.; Rodriguez, M.; Gaus, K. PALM Imaging and Cluster Analysis of Protein Heterogeneity at the Cell Surface. *J. Biophotonics* **2010**, *3* (7), 446–454.

(85) Ober, R. J.; Ram, S.; Ward, E. S. Localization Accuracy in Single-Molecule Microscopy. *Biophys. J.* **2004**, *86* (2), 1185–1200.